### Title
Quantitative contrast-enhanced spectral mammography based on photon-counting detectors: A feasibility study




### Journal
Medical Physics, 44(8)

### ISSN
0094-2405



### Authors
Ding, Huanjun
Molloi, Sabee



### Publication Date
2017-08-01

### DOI
10.1002/mp.12296

Peer reviewed

# Quantitative contrast-enhanced spectral mammography based on photon-counting detectors: A feasibility study

Huanjun Ding and Sabee Molloi[a)]
*Department of Radiological Sciences, University of California, Irvine, CA 92697, USA*

(Received 13 April 2016; revised 12 April 2017; accepted for publication 14 April 2017; published 28 June 2017)

**Purpose:** To investigate the feasibility of accurate quantification of iodine mass thickness in contrast-enhanced spectral mammography.

**Materials and methods:** A computer simulation model was developed to evaluate the performance of a photon-counting spectral mammography system in the application of contrast-enhanced spectral mammography. A figure-of-merit (FOM), which was defined as the decomposed iodine signal-to-noise ratio (SNR) with respect to the square root of the mean glandular dose (MGD), was chosen to optimize the imaging parameters, in terms of beam energy, splitting energy, and prefiltrations for breasts of various thicknesses and densities. Experimental phantom studies were also performed using a beam energy of 40 kVp and a splitting energy of 34 keV with 3 mm Al prefiltration. A two-step calibration method was investigated to quantify the iodine mass thickness, and was validated using phantoms composed of a mixture of glandular and adipose materials, for various breast thicknesses and densities. Finally, the traditional dual-energy log-weighted subtraction method was also studied as a comparison. The measured iodine signal from both methods was compared to the known value to characterize the quantification accuracy and precision.

**Results:** The optimal imaging parameters, which lead to the highest FOM, were found at a beam energy between 42 and 46 kVp with a splitting energy at 34 keV. The optimal tube voltage decreased as the breast thickness or the Al prefiltration increased. The proposed quantification method was able to measure iodine mass thickness on phantoms of various thicknesses and densities with high accuracy. The root-mean-square (RMS) error for cm-scale lesion phantoms was estimated to be 0.20 mg/cm$^2$. The precision of the technique, characterized by the standard deviation of the measurements, was estimated to be 0.18 mg/cm$^2$. The traditional weighted subtraction method also predicted a linear correlation between the measured signal and the known iodine mass thickness. However, the correlation slope and offset values were strongly dependent on the total breast thickness and density.

**Conclusion:** The results of this study suggest that iodine mass thickness for cm-scale lesions can be accurately quantified with contrast-enhanced spectral mammography. The quantitative information can potentially improve the differential power for malignancy.  [https://doi.org/10.1002/mp.12296]

Key words: contrast-enhanced spectral mammography, dual energy, material decomposition

## 1. INTRODUCTION

In recent decades, early detection of breast cancer has been substantially improved through technical advances in digital mammography.[1,2] However, it has been shown that digital mammography is less sensitive in detecting tumors with dense breasts.[3] In addition, mammography's positive predictive value remains as low as 20%,[4–8] which contributes to the large number of false-positive findings in biopsies recommended after mammography. It has been reported that up to 60% of women undergoing annual screening mammography over 10 yr will have at least one false-positive mammography result.[9,10] Conventional mammography's limited specificity can subject many healthy women to unnecessary additional radiation or needle biopsies and increase healthcare costs. To address this limitation, complementary breast imaging techniques, such as breast tomosynthesis[11,12] and breast computed tomography (CT),[13–16] have been investigated to increase lesion detectability, especially for dense breasts. However, the ability to differentiate benign from malignant lesions may be fundamentally limited by small differences in X-ray attenuation coefficients of tumors and normal breast tissues.[17] A potential solution in breast cancer diagnostic work-up is contrast-enhanced imaging, which characterizes breast lesions by examining neoangiogenically induced vascular changes and has demonstrated encouraging results in detecting breast cancer.[18–20]

Contrast-enhanced spectral mammography has been recently introduced into clinical practice for diagnostic breast imaging. Due to the requirement of contrast injection, it is typically not used for general breast screening. However, studies have suggested promising future applications in diagnostics, therapy follow-up, and 'high-risk' patient screening.[21–23] Clinical studies have suggested that the lesion detection capability is significantly superior for contrast-enhanced mammography than conventional mammography

and ultrasound using BI-RADS lexicon in the diagnostic workup.[24,25] A recent study suggested that when used with conventional mammography, contrast-enhanced mammography was able to increase the sensitivity in detecting malignancies from 78% to 93%.[25] Despite this notable improvement in sensitivity, the specificity for the probability of malignancy remains about the same as conventional mammography, which is approximately 50% to 68%.[25,26] To address the relatively poor specificity, one needs to establish the correlation between the quantitative information from contrast-enhanced mammograms and the pathological parameters of malignant lesions. However, standard contrast-enhanced spectral mammography technique relies on the weighted log subtraction of the dual-energy images.[27] This method is effective in minimizing the background anatomical noise, which improves the sensitivity in lesion detection. However, due to the polyenergetic nature of the x-ray spectrum, the linear subtraction method cannot adequately address the nonlinear process during dual-energy imaging, such as beam hardening and scatter. As a result, it has very limited accuracy in quantitative analysis. In addition, due to the signal superposition in mammography, the background breast tissue contributes to a large portion of the subtracted signal, which may vary substantially depending on the breast thickness and density. Therefore, the quantitative information is not readily available for the comparison among different lesions. There are few studies that investigate this issue based on clinical data. In a very recent study involving 174 women,[28] the relationships between enhancement in contrast-enhanced spectral mammography and blood vessel density, lymphatic vessel density, and other related parameters obtained from immunohistochemistry were assessed. The authors reported that the sensitivity of detection of malignant lesions for contrast-enhanced spectral mammography was 100%, while the specificity remained at 39%. The immunohistochemistry results suggested that blood vessel density is an excellent biomarker to differentiate between malignant and benign lesions. However, the correlation between enhancement in contrast-enhanced spectral mammography and the blood vessel density was relatively poor with a Spearman's correlation coefficient of 0.357.[28] This is likely due to the difficulty of quantitative characterization on enhancement with the projection images using current method. In addition, enhancement observed in contrast-enhanced mammography may also be related to functional parameters such as vessel permeability.[29] Thus, these findings suggest clinical applications in quantitative contrast-enhanced spectral mammography, for which an accurate measure of the iodine mass thickness inside the lesion can be provided for breasts of various thicknesses and fibroglandular tissue densities. This quantitative metric is expected to correlate strongly with the pathological parameters of lesions such as vascular density, permeability, and perfusion. It can potentially serve as an imaging biomarker to improve the differentiation power for malignancy.

Contrast-enhanced spectral mammography requires the acquisition of two independent images at low- and high-energy windows. The traditional approach is based on the dual-kVp method, where two exposures are made sequentially with a minimal delay time.[20] Recent advances in spectral mammography systems based on Si-strip photon-counting detectors offer the capability to acquire dual-energy images simultaneously within a single exposure.[30–34] This is achieved through the photon-counting detectors, which can sort incoming photons according to their energies. In addition, the photon-counting spectral mammography system has a scanning multislit geometry that can eliminate the scattered radiation.[32] The effective scatter rejection not only reduces the radiation dose to patients but also improves the accuracy in quantitative material decompositions. An energy-resolved photon-counting spectral mammography system was used in this study. In contrast-enhanced mammography, the primary imaging task is to maximize the signal from iodinated contrast agent, which has a k-edge at 33.2 keV. Thus, it will be favorable to use much higher beam energy and thicker prefiltration than what is used in the conventional mammography, in which a softer beam is commonly used to optimize the contrast between soft tissues in low energy. Thus, it is necessary to investigate the feasibility of optimizing the x-ray spectra that is used for contrast-enhanced spectral mammography.

In this article, we will first evaluate the optimal imaging parameters, in terms of beam energy, splitting energy, and prefiltration, for a photon-counting spectral mammography system toward the application of contrast-enhanced spectral mammography. A set of imaging parameters was suggested in a previous study.[35] However, we will provide a more comprehensive simulation study, which investigates the effects of breast thickness and density, and explores the potential gain beyond the hardware limitations from the current system. Secondly, as the main focus of the study, we will present a novel method to accurately quantify iodine mass thickness signal in contrast-enhanced spectral mammography using the optimal imaging parameters predicted in the previous simulation studies. Phantom studies have been designed to evaluate the accuracy and precision of the proposed technique with respect to the ground truth. For comparison, the results from the conventional weighted subtraction method will also be presented. Finally, the potential application of the proposed quantification method will be discussed.

## 2. MATERIALS AND METHODS

### 2.A. Analytic simulation model

A previously reported analytical model was modified for simulation of contrast-enhanced spectral mammography.[36] The simulation traces the emission of photons from the x-ray source, their attenuation through the patient, and subsequent absorption in the detector. From this ray tracing, the x-ray attenuation coefficients of a given breast composition were calculated for both low- and high-energy bins, as were the recorded detector signals and their uncertainties due to quantum noise. These quantities were used to further calculate additional figures relevant to dual-energy material decomposition, such as the dual-energy decomposed iodine signal and noise.

The simulation used polyenergetic x-ray spectra from a tungsten-anode x-ray tube, which were generated by the TASMIP code.[37] We varied the beam energy from 20 to 120 kVp in intervals of 1 kVp. The upper limit of the beam energy selection is far beyond the traditional energy range for mammography. However, the range of the simulation was selected to first evaluate the global maximum, while allowing the parameters to change freely within a relatively large range. The simulation will then determine a practical maximum after considering the current hardware limitations, and evaluate the benefit-to-cost profile for this specific imaging task. The splitting energy, defined as the high-energy threshold that separates low- and high-energy photons, is an essential imaging parameter for spectral imaging using photon-counting detectors. This is especially true for contrast-enhanced spectral mammography, due to the presence of the iodine k-edge at 33.2 keV. In the simulation, the splitting energy increased from 10 keV to the maximum value in a given spectrum with a step of 1 keV for each beam energy. The effective prefiltration, which includes the attenuation from the filter and compression paddle, was simulated using an Al filter. The initial effective Al filter thickness was set at 0.75 mm, which matched the equivalent prefiltration in the conventional spectral mammography system. The effect of prefiltration was studied by increasing the Al filter thickness up to 3 mm, which sets the upper limit for tube loading considerations.

The breast was modeled as a mixture of the adipose and mammary gland tissues with a breast density of 30%, which is close to the most recent estimates of clinical breast density.[38] Breast thickness varied from 2 to 8 cm, which covers the clinical range for compressed breasts. A 4-mm iodine signal with concentrations ranging from 2 to 8 mg/ml, which have been found reasonable for tumor uptake,[19,35] was used to simulate a lesion.

The simulated detector was a Si-based photon-counting detector. The detector response function was assumed to have an ideal energy resolution without the presence of pulse pileup or charge sharing. The quantum detection efficiency (QDE) of the detector was estimated from the x-ray attenuation property of a 3.6-mm-thick Si crystal, which is consistent with the effective thickness of the Si-strip detector in the spectral mammography system. No additive electronic noise was included in the simulation, due to the nature of photon-counting detectors. Effects from x-ray scatter were not included in the simulation due to the effective scatter rejection from the multislit geometry.

For each imaging protocol, i.e., the combination of beam energy, splitting energy, and prefiltration, the dual-energy signal-to-noise ratio for iodine ($SNR_I$) was solved analytically using the attenuation coefficients of glandular, adipose, and iodine, the known total breast thickness, and the SNR of low- and high-energy images.[37] Using a previously developed analytical method for three-material decomposition,[39] the iodine SNR was calculated from the uncertainty in the decomposed basis material thickness measurement. As the signal is normalized to the known input of iodine thickness, the SNR is basically calculated from the variance in thickness measurement. The detailed derivation of the thickness variance can be found in previous reports.[39,40] Mean glandular dose ($MGD$) was calculated using previously reported data generated from the Monte Carlo simulations for each thickness and density combination used in the simulation.[41,42] Finally, a figure-of-merit ($FOM$) was calculated to optimize the dual-energy SNR with respect to patient dose, and was defined as:

$$FOM = \frac{SNR_I}{\sqrt{MGD}} \quad (1)$$

This definition permits an easy comparison of the image qualities of the different configurations. The simulation was first performed with 0.75-mm Al prefiltration for breasts with different thicknesses in the range 2–8 cm with a fixed density of 30%. The optimal image parameters were determined by maximizing the FOM. The second simulation was based on a 4 cm breast with 30% density, and investigated the optimal imaging parameters when the Al prefiltration increased from 0.75 to 3 mm.

## 2.B. Spectral mammography system

A spectral mammography system (MircoDose SI L50, Phillips Inc.) was used in the experimental studies. The system is based on Si-strip photon-counting detectors, which are able to register individual photons and sort them into the low- and high-energy bins according to their energies. The system consists of a tungsten-anode x-ray tube, an Al filter, a pre- and a postcollimator, and the Si-strip photon-counting detector unit, which are all mounted on a common arm that can rotate around the center of the source, allowing the collimators and the photon-counting detector to scan relative to the compressed breast. The detector's energy resolution at the mammography energy range is approximately 5 keV at full width half maximum (FWHM).[43] The electronic readout noise is effectively eliminated by proper selection of the background threshold, which improves detection efficiency, especially for low-dose applications. A multislit collimator shapes the beam to match the detector, and a two-dimensional image is generated when the beam and detector are scanned relative to the breast. The scanning multislit technique helps to eliminate scattered radiation, which remains a major limitation for charge-integrating flat-panel detectors. A previous study suggests that the scatter to primary ratio (SPR) for this geometry is expected to be less than 6% for phantom thicknesses ranging from 3 to 7 cm at various tube voltages.[31] More details about the spectral mammography system can be found in a previous publication.[36]

## 2.C. Theory for quantitative contrast-enhanced spectral mammography

Previous studies have addressed the fundamental physics for contrast-enhanced spectral mammography.[20,35] In general, contrast-enhanced mammography involves three basis

materials: adipose, fibroglandular, and iodine. With dual-energy imaging, it would normally be impossible to accurately measure the thickness of these three basis materials simultaneously, due to the lack of an additional constraint. Therefore, the current contrast-enhanced spectral mammography technique, using weighted dual-energy subtraction method, aims to improve the detectability of the iodine signal by eliminating the background anatomical noise. However, the resulting iodine signal may not have a direct correlation with the true iodine mass thickness in the lesion. This study proposes a simple method to establish this correlation, so that the enhancement of a lesion can be quantified using iodine mass thickness.

Using a two compartment model for breast, the logarithmic signal ($I$) of normal breast tissue in mammography can be written as a combination of adipose ($a$) and glandular ($g$) contents:

$$\begin{pmatrix} \mu_g^L & \mu_a^L \\ \mu_g^H & \mu_a^H \end{pmatrix} \begin{pmatrix} t_g \\ t_a \end{pmatrix} = \begin{pmatrix} lnI_L \\ lnI_H \end{pmatrix} \tag{2}$$

where $\mu$ and $t$ are the energy-dependent X-ray attenuation coefficient and the effective thickness for each type of tissue, respectively. $L$ and $H$ denote the low- and high-energy images, respectively. After contrast administration, iodine also contributes to the measured signal ($I'$), if it is presented in a lesion. However, the additional iodine volume is very small, so we can approximate that the original breast tissue composition remains intact, i.e.,:

$$\begin{pmatrix} \mu_g^L & \mu_a^L & \mu_i^L \\ \mu_g^H & \mu_a^H & \mu_i^H \end{pmatrix} \begin{pmatrix} t_g \\ t_a \\ t_i \end{pmatrix} = \begin{pmatrix} lnI'_L \\ lnI'_H \end{pmatrix} \tag{3}$$

Here, the effective thicknesses of glandular and adipose tissues ($t_g$ and $t_a$) can be assumed to be the same as those in Eq. (2) before contrast injection. We have previously demonstrated that dual-energy/spectral mammography can be used to solve for Eq. (2), resulting in an accurate quantification of glandular and adipose tissue thicknesses.[36,44,45] At the same time, by adding the thickness images of both glandular and adipose tissues, a total breast thickness ($T$) image can be obtained, where the density component is completely removed from the image. The signal ($S$) on this thickness image can be written as:

$$S = t_g + t_a = T \tag{4}$$

This allows the elimination of the background anatomical noise induced by the contrast between glandular and adipose tissue, and resulted in a slowly varying thickness profile of the breast. For a compressed breast, a large portion of the pixels will have approximately the same value, while $T$ gradually decreases toward the periphery. When iodine is present during the dual-energy decomposition, the third term in Eq. (3) will introduce an additional signal in the decomposed thickness image. The total attenuation of iodine will be decomposed into the two basis materials, resulting in contrast-based thicknesses of glandular ($t_g'$) and adipose ($t_a'$). For a given input spectrum, breast thickness, and density, the effective attenuation of iodine ($\mu_i$) can be written as a linear combination of glandular and adipose:

$$\begin{pmatrix} \mu_g^L & \mu_a^L \\ \mu_g^H & \mu_a^H \end{pmatrix} \begin{pmatrix} x_1 \\ x_2 \end{pmatrix} = \begin{pmatrix} \mu_i^L \\ \mu_i^H \end{pmatrix} \tag{5}$$

where $x_1$ and $x_2$ are dual-energy decomposition coefficients for the selected basis material. Therefore, the correlation between the true iodine thickness ($t_i$) and the contrast-induced thicknesses of glandular ($t_g'$) and adipose ($t_a'$) for a given attenuated spectrum can be written as:

$$\begin{pmatrix} t'_g \\ t'_a \end{pmatrix} = \begin{pmatrix} x_1 \\ x_2 \end{pmatrix} t_i \tag{6}$$

In this context, the measured enhancement in the decomposed thickness image is expressed as:

$$S = t_g + t_a + t'_g + t'_a = T + (x_1 + x_2)t_i = T + st_i \tag{7}$$

This simple model predicts the following conclusions. First, from Eq. (7), it is observed that the measured enhancement in the dual-energy decomposed total thickness image is linearly related to the true iodine thickness for a given spectrum. Second, the offset of this linear correlation is the physical breast thickness, or the thickness measured on unenhanced breast tissue. Finally, the slope ($s$) in this correlation is not a constant. It depends on the attenuation spectrum, which is a function of input spectrum, breast thickness, and density. Unlike conventional mammography where imaging protocol varies significantly depending on breast compression thickness, the imaging parameters of contrast-enhanced mammography may be almost independent of breast size, as suggested by our simulation results. Thus, the slope can be treated as a function of breast thickness ($T$) and density ($D$). If a definite function or a lookup table can be generated, which accurately predicts the slope ($s$) in Eq. (7) from the measurements of breast thickness ($T$) and density ($D$), the enhancement in dual-energy decomposed image can then be converted into true iodine thickness. Following our previous calibration method for breast density quantification, we will use a nonlinear rational function to characterize this correlation.[36] This function has been validated in previous dual-energy breast density quantification studies, which have demonstrated its accuracy for nonlinear surface fitting.[36]

$$s = \frac{a_0 + a_1{*}\mathrm{T} + a_2{*}\mathrm{D} + a_3{*}\mathrm{T}^2 + a_4{*}\mathrm{T}*\mathrm{D} + a_5{*}\mathrm{D}^2}{1 + b_1{*}\mathrm{T} + b_2{*}\mathrm{D}} \tag{8}$$

In summary, the true iodine thickness ($t_i$) can be expressed as a function of the enhancement in the total breast thickness image ($S$), the breast thickness ($T$), and density ($D$) at the site of enhancement. Although $S$ can be easily obtained, it is impossible to directly measure $T$ and $D$, as the pixel value at the site of enhancement is the combination of unenhanced tissue thickness and contrast-induced thickness signal. To mitigate this issue, we will use the tissue thickness and

composition measurements from an adjacent area where no contrast enhancement is observed. One assumption used here is that the iodine uptake in the normal tissue is much less, comparing to that in a lesion, and the small uptake in the normal tissue can be canceled out when the integrated signal on top of the lesion is subtracted by the signal from the surrounding area. In the above method, the background tissue thickness and density are used to determine the conversion slope ($s$). Iodine uptake in normal tissue may introduce errors in the dual-energy decomposition, which generally leads to an overestimation of the tissue thickness ($T$). However, the enhancement in the total breast thickness image in the lesion ($S$) is also affected by the normal tissue uptake below and above the lesion. If we can assume a similar normal tissue composition around the lesion, thus a similar iodine uptake in the normal tissue, the errors induced by the normal tissue uptake can be largely canceled when we derive the iodine thickness ($t_i$) based on the signal difference between the enhancement in a lesion ($S$) and the background tissue thickness ($T$) using Eq. (7). The conversion slope ($s$) is also affected by the estimation of the background tissue thickness. However, it should be noted that the error in iodine quantification induced by the deviation of the conversion slope can be largely offset by the overestimation in the enhancement signal on the lesion ($S$). A more detailed sensitivity analysis will be provided in the following sections to address this issue.

### 2.D. Dual-energy calibration

Following the method discussed in the previous section, a two-stage dual-energy calibration was used to determine the system parameters for iodine mass thickness quantification in contrast-enhanced spectral mammography. The initial calibration is identical to our previously reported dual-energy breast density calibration.[36] Glandular and adipose tissue equivalent plastic phantoms of uniform thickness (CIRS, Norfolk, VA) were used for dual-energy calibration. All phantoms had the same dimensions of $10.0 \times 12.5$ cm$^2$. Three thicknesses (0.5, 1.0, and 2.0 cm) were available. The maximum possible thickness for each phantom material was 8.5 cm. The known breast densities were determined by the thickness percentages of the glandular phantom. The change in breast density was achieved by varying the combination of glandular and adipose phantoms. Fifteen calibration points were selected to cover the full range of clinically relevant breast thicknesses and densities, shown in Table I.[36] In addition, open-field images were acquired during the calibration and were used to produce normalized logarithm-transformed images for the attenuation estimation. The known thickness values for each type of phantom and the corresponding dual-energy attenuation measurements were fitted with a nonlinear rational function.[36] The system calibration parameters for each material were then determined separately from a nonlinear least-squares minimization algorithm.[46] In the following dual-energy decomposition process, these parameters were used to estimate the thickness values of the corresponding phantoms, with the measured dual-energy signals. A more detailed description of this calibration step can be found in a previous report.[36]

The initial dual-energy breast density calibration allows for accurate quantification of total breast thickness and density. Both figures are important for the secondary calibration, which aims to predict the correlation between the conversion slope ($s$) in Eq. (7) and breast thickness and density. This step was completed using iodine disk phantoms with volumetric concentrations of 2, 2.5, 5, 7.5, 10, and 20 mg/ml of iodine. The iodine disk phantoms have a height of 5 mm, which were customized from iodine inserts of a commercial dual-energy CT phantom (Gammex, Inc., Middleton, WI, USA). The iodine disks were embedded in an adipose slab with uniform thickness of 5 mm, so that the total thickness was constant across the phantom. Six iodine phantoms of various concentrations were imaged in combination with the glandular and adipose slab phantoms used in the initial breast density calibration at each of the 15 calibration points, yielding a total of 90 measurements. Dual-energy images of the iodine disks were decomposed using the system parameters obtained from the initial breast density calibration. The total thickness image and the density image were calculated using the decomposed glandular and adipose thickness images. For each of the 15 calibration points with a distinct phantom configuration in terms of total thickness and density, the signal from the total thickness images for each iodine disk was measured and plotted as a function of the known iodine mass thickness. A linear fitting was performed for each dataset to derive the offset and the slope values, shown in Table I. The slopes and the known background phantom configurations in terms of total thickness and density were then substituted into Eq. (8) to determine the fitting parameters ($a_0$, $a_1$,...) using a least-squares minimization algorithm.

TABLE I. List of 15 calibration points and the conversion slope and offset values from the linear fitting.

| Calibration points | Thickness (cm) | Density (%) | Conversion slope (cm$^3$/mg) | Offset (cm) |
|---|---|---|---|---|
| 1 | 1.0 | 100 | 0.85 | 1.51 |
| 2 | 2.0 | 100 | 0.89 | 2.54 |
| 3 | 4.0 | 100 | 0.98 | 4.55 |
| 4 | 6.0 | 100 | 1.09 | 6.54 |
| 5 | 8.0 | 100 | 1.30 | 8.38 |
| 6 | 1.0 | 0 | 0.80 | 1.49 |
| 7 | 2.0 | 0 | 0.87 | 2.51 |
| 8 | 4.0 | 0 | 0.92 | 4.53 |
| 9 | 6.0 | 0 | 1.00 | 6.53 |
| 10 | 8.0 | 0 | 1.09 | 8.54 |
| 11 | 2.0 | 50 | 0.86 | 2.55 |
| 12 | 3.0 | 50 | 0.93 | 3.52 |
| 13 | 4.0 | 50 | 0.94 | 4.52 |
| 14 | 6.0 | 50 | 1.07 | 6.55 |
| 15 | 8.0 | 50 | 1.16 | 8.63 |

### 2.E. Validation study using BR3D phantoms

To validate the proposed method, phantom studies were designed using a mammographic phantom with a heterogeneous pattern (BR3D, CIRS, Norfolk, VA, USA) as the background to simulate the anatomical noise in clinical mammograms. The BR3D phantom is constructed with a swirled pattern of adipose and glandular tissue equivalent materials with an overall 50–50 ratio. The random swirling pattern varies the local glandularity depending on the position of the phantom. The iodine phantoms used in the calibration, with an addition of a 15 mg/ml disk, were imaged with the BR3D phantoms of various thicknesses, ranging from 2 to 5 cm. This setup allows the investigation of quantification accuracy as a function of background thickness and density. The acquired dual-energy images were decomposed using the initial breast density calibration, yielding the total thickness and density images. A ring region-of-interest (ROI) was placed near the iodine disks to measure the background thickness and density, which were used as the inputs in Eq. (8) for the estimation of the conversion slope. Finally, the iodine mass thickness was determined through Eq. (7) with the calculated slope and offset values.

To compare with the conventional approach in contrast-enhanced spectral mammography, a dual-energy log-subtraction method, using a weighted linear combination, was also performed on the validation images.[35] The proper weighting factor was determined based on the following equation:

$$w = \frac{\mu_g^L - \mu_a^L}{\mu_g^H - \mu_a^H} \tag{9}$$

where the low- and high-energy attenuation coefficients of the glandular and adipose phantoms were obtained through a system calibration using the same dataset from the initial breast density calibration. Signals from the iodine disks were measured in the dual-energy subtracted images for each background phantom thickness.

The contrast-to-noise ratio (CNR) was measured on the dual-energy decomposed images using circular ROIs, which are approximately 1.5 cm in diameter. The mean and standard deviation of the ROIs placed on the iodine disks and the BR3D background were recorded. The CNR was calculated using the following equation:

$$CNR = \frac{S_I - S_B}{\sigma_B} \tag{10}$$

where $S_I$ and $S_B$ were the mean signal in iodine and background ROIs, and $\sigma_B$ was the standard deviation in the background ROI.

All phantom images were acquired at 40 kVp and 7.5 mAs. The splitting energy was set at 34 keV. Additional 3 mm Al filter was added to the existing system. The exposure of the system at these settings was carefully measured using an ion chamber (Model 2026C, Radcal Corporation, Monrovia, CA, USA). The exposure level used in this study corresponded to an estimated MGD of approximately 0.17 mGy, which was estimated based on a previous Monte Carlo simulation for a 4 cm breast with 50% density.[34,35]

### 2.F. Statistical analysis

The calculated iodine mass thickness obtained from the dual-energy decomposition was compared to the known values of the iodine disks. Linear regression analysis was performed to characterize the correlation between the measured and the known values. The absolute error in mass thickness was calculated for each iodine phantom at every breast phantom thickness. Root-mean-square (RMS) error was used to quantify the accuracy of the measurements. The precision of the technique, which is defined as the variance induced by changes in breast thickness and density, was also calculated for each iodine mass thickness.

A sensitivity study was designed to address the potential uncertainty in thickness estimation induced by normal tissue iodine uptake. As it is generally difficult to accurately estimate the uncertainty, we simply assumed a percent error in thickness estimation, which ranges between 5 and 40% for a 4 cm background, yielding a thickness uncertainty between 2 to 16 mm. The affected conversion slopes were calculated based on each percent error level of the background thickness. In the mean time, it is assumed that the normal tissue uptake is the same for tissues around the lesion, and the same percent error level was assigned for the enhanced signal in the lesion. Finally, for each level of percent error in background thickness, the iodine quantification error was derived using the RMS error of a set of iodine mass thickness in the range of 1 to 10 mg/cm$^2$. The correlation between iodine quantification error and the background thickness uncertainty was studied.

## 3. RESULTS

The 2D contour plot of the FOM as a function of the beam energy and the splitting energy for the investigated photon-counting spectral mammography system is shown in Fig. 1. The simulation was carried out for a 4-cm-thick breast with breast density of 30%. A prefiltration of 0.75 mm Al was used, which matched the equivalent prefiltration of the clinical spectral mammography system. The optimal imaging protocol, which leads to the highest FOM, can be found at a beam energy of 45 kVp with a splitting energy at 34 keV. A more detailed analysis is shown in Fig. 2, where the FOM is plotted as a function of the splitting energy for various beam energies, including 38, 40, and 45 kVp. Here, all FOM values were normalized by the maximum at 45 kVp. It can be seen that the simulated FOM values depend strongly on the selection of the splitting energy. The curves peaked at 34 keV, noted by the dashed line in the plot, and decreased abruptly on both sides, for all tube voltages. However, FOM is relatively insensitive to the beam energy. It was only reduced by approximately 7% when the tube voltage decreased to 40 kVp, which is the maximum beam energy of

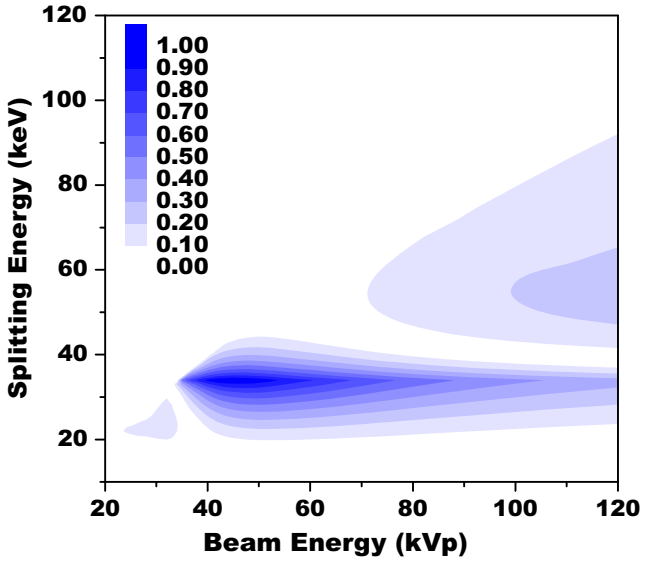


FIG. 1. 2D contour plot of the FOM as a function of the beam energy and the splitting energy for a 4 cm breast with 30% density. [Color figure can be viewed at wileyonlinelibrary.com]

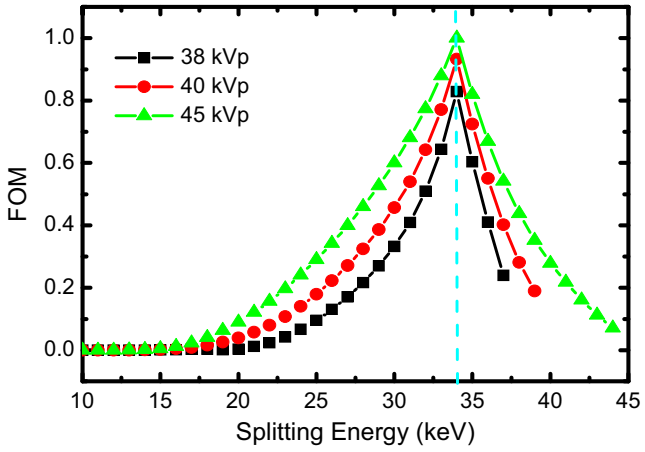


FIG. 2. FOM as a function of the splitting energy for various beam energies for a 4 cm breast with 30% density. [Color figure can be viewed at wileyonlinelibrary.com]

the investigated spectral mammography system. The FOM simulations were performed for breasts of different thicknesses with a fixed breast density at 30%. As shown in Fig. 3(a), in general, FOM decreased as the breast became thicker. The optimal beam energy varied slightly from 46 to 44 kVp, while the splitting energy remained at 34 keV. The effect of prefiltration was also simulated for a 4 cm breast with 30% density, as shown in Fig. 3(b). As the Al filter thickness started to increase from 0.75 mm, the iodine detection efficiency improved monotonically. This is most attributed to the improved dose efficiency in the FOM calculation. At the same time, the optimal tube voltage decreases toward 42 kVp. This is also expected, as a narrow spectrum around the k-edge of iodine would provide the best discrimination power between iodine and breast tissue.

The unattenuated spectra at 40 kVp with 0.75 and 3 mm Al prefiltrations are shown in Fig. 4, along with the latter one after being attenuated by thin, average, and large breasts. The two unattenuated spectra were normalized to their maximum intensities. The above simulation results suggested that, compared to conventional mammography, higher tube voltages are preferred for contrast-enhanced spectral mammography. More importantly, the setting of the high-energy threshold, which serves as the splitting energy, needs to match the k-edge of iodine. Due to hardware limitations, the experimental system has a maximum tube voltage of 40 kV. However, the loss in FOM due to this reduction in beam energy is only a few percentages. Furthermore, this FOM loss can be compensated by increasing the Al filter thickness. These findings provided critical guidelines for the following experimental study.

The dual-energy calibration process is shown in Fig. 5 and the primary results are summarized in Table I. After dual-energy data acquisition, the images were converted into thickness and glandularity maps using a previously reported breast density quantification method.(citation) The thickness signal of iodine targets measured on a 4 cm background is plotted as a function of iodine density in Fig. 5(a). A linear correlation can be derived from this dataset as one would expect from Eq. (7). For all the background thickness and density combinations used in the calibration, the slope and the offset of the linear fitting were recorded in Table I. For all 15 calibration points, the linear correlation coefficients ($r^2$) for this fitting are above 0.99, suggesting a reliable linear correlation between the decomposed thickness signal and the known iodine mass thickness as predicted in Eq. (7). It can be noted that the conversion slope varied from 0.8 to 1.3, depending on the background phantom configuration. The uncertainties in the fitted slopes ranged between 0.01 and 0.02 $cm^3$/mg. In general, the slope increased as the attenuation of the background phantom increased. For thinner background, this trend appeared noisy, due to the larger relative errors in dual-energy decomposition for the total thickness estimation, which is consistent with previous reports.[36] As shown in Eq. (7), the offset values should match the total thickness of the phantom. Considering the 5 mm additional thickness of the iodine phantom on top of the background thickness, the fitted offset values agreed closely with our prediction. As shown in Fig. 5(b), the known background thickness and density, along with the measured conversion slopes, were used in the secondary calibration using Eq. (8) to find the system parameters. With the surface function shown in the plot, the conversion slope can be determined for any mammogram, as long as the breast thickness and density can be measured using dual-energy decomposition.

A photo of the iodine insertion and the BR3D background phantoms is shown in Fig. 6(a). The log-transferred phantom images for contrast-enhanced spectral mammography are also shown in Fig. 6, which compares the conventional single-energy mammogram (b), the dual-energy decomposed total thickness image (c), and the traditional weighted subtraction image (d). The large iodine disk phantoms shown in these

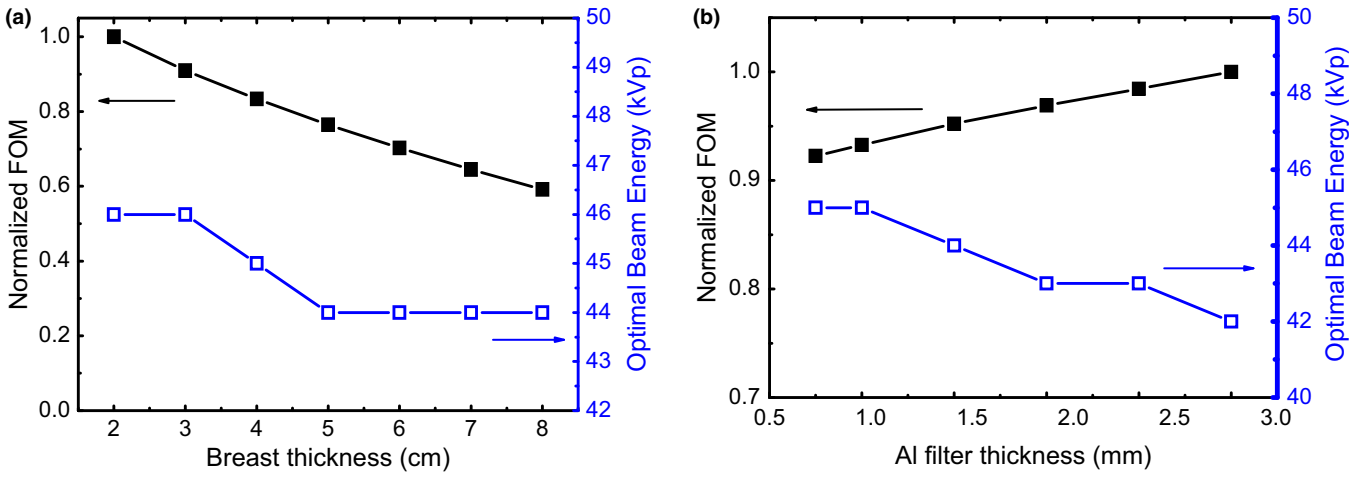


FIG. 3. (a) The simulated FOM and the optimal beam energy for various breast thicknesses with 30% breast density and 0.75 mm Al prefiltration; and (b) The effect of Al prefiltration for 4 cm breast with 30% density. [Color figure can be viewed at wileyonlinelibrary.com]

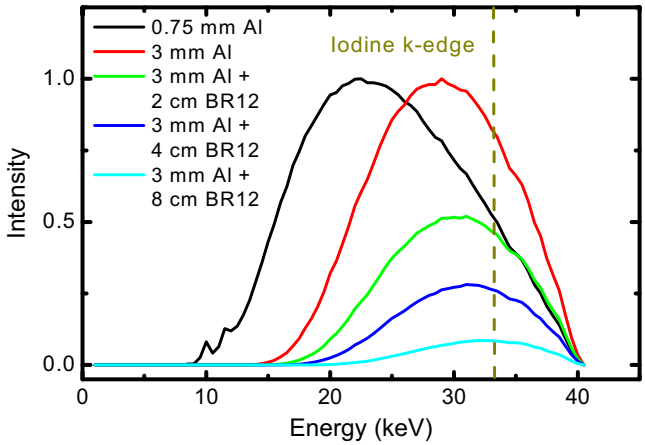


FIG. 4. The unattenuated spectra at 40 kVp with 0.75 and 3 mm Al prefiltrations, along with the latter one after being attenuated by thin, average, and large breasts. The two unattenuated spectra were normalized to their maximum intensities. [Color figure can be viewed at wileyonlinelibrary.com]

images have mass thickness of 2.5 and 10 mg/cm$^2$. As all three images were obtained from a single exposure, the radiation dose was exactly the same. It can be seen that the dual-energy decomposition greatly suppressed the anatomical noise in the background. This is particularly true for the proposed nonlinear calibration method (c), while some background noise still remains in the linear subtraction method (d). The uniform background significantly improves the visibility of the iodine signal, especially for small targets with low iodine thicknesses. When comparing the two dual-energy decomposition techniques, due to its limited capability in suppressing noise and its relatively poor accuracy in estimating thickness, the linear subtraction method failed to detect an iodine thickness of 2.5 mg/cm$^2$ even for a large disk. This is mostly due to the small signal difference between the iodine and the background. The CNR of the large iodine disk phantoms with various iodine mass thicknesses is plotted in Fig. 7. As compared to the standard single-energy image, the proposed dual-energy decomposition improved CNR by a factor of 2 on average. The linear log-subtraction method does not gain much in CNR comparing to single-energy image. This is not only because of the small signal difference after log subtraction but also due to the remaining structural noise in the background which was not completely removed using the linear method.

Using the proposed methods, the iodine mass thicknesses were determined in the validation phantom study and compared to the known values in Fig. 8. The iodine disks in this measurement were placed randomly at different locations on BR3D phantoms so the background density varied from approximately 10% to 75% and the total breast thickness varied from 2 to 5 cm. Thus, there were four measurements for each iodine mass thickness value, and those measurements were made at different breast thicknesses and densities. The mean and the standard deviation of these four measurements were calculated and shown in Fig. 8 as the solid squares and the error bars, respectively. A linear fitting between the measured and the known iodine mass thickness values resulted in a slope of 1.01 and an offset of −0.18 mg/cm$^2$. The Pearson's r was estimated to be 0.99. Compared to the known values, the RMS error was estimated to be approximately 0.20 mg/cm$^2$, which characterized the accuracy of the proposed quantification technique. The precision was characterized by the average standard deviation of each measurement, which was estimated to be 0.18 mg/cm$^2$.

The results using the traditional weighted log-subtraction method are also shown in Fig. 9 for comparison. With an optimal weighting factor, the linear subtraction method was also able to largely remove the background noise in the dual-energy log-subtracted image. The signal measured on the subtracted images was found to be linearly correlated with the known iodine mass thickness. However, as the background phantom thickness varied, this correlation changed systematically. As the subtracted signal does not have physical meaning, we presented the results in terms of CNR as a function of the known iodine mass thickness, so that the

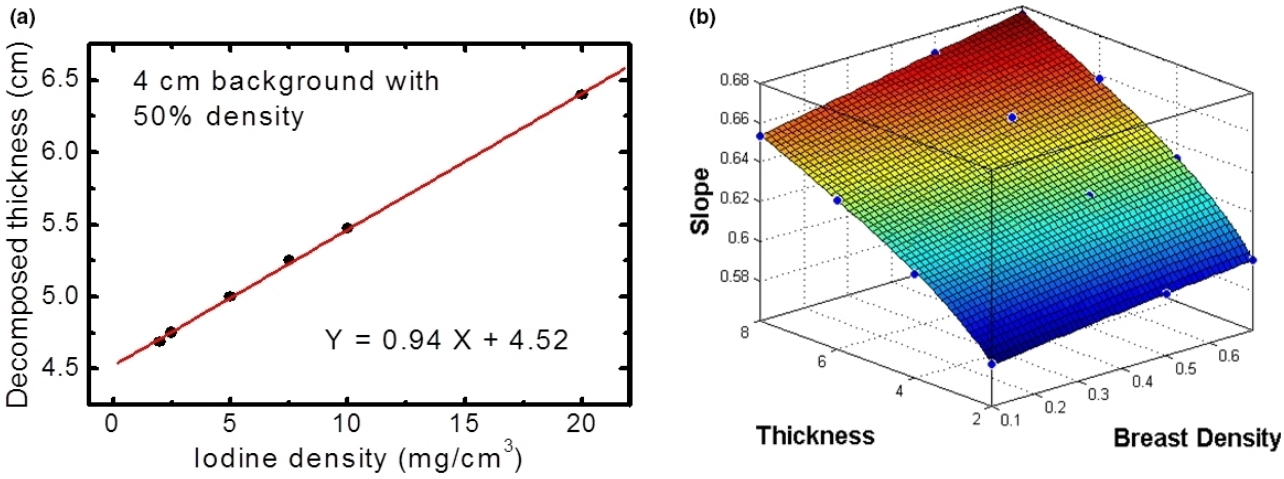


FIG. 5. (a) Linear fitting of the decomposed thickness signal as a function of the known iodine density for a 4 cm phantom with 50% glandularity. (b) Nonlinear fitting of the iodine conversion slopes as functions of background breast density and thickness. [Color figure can be viewed at wileyonlinelibrary.com]

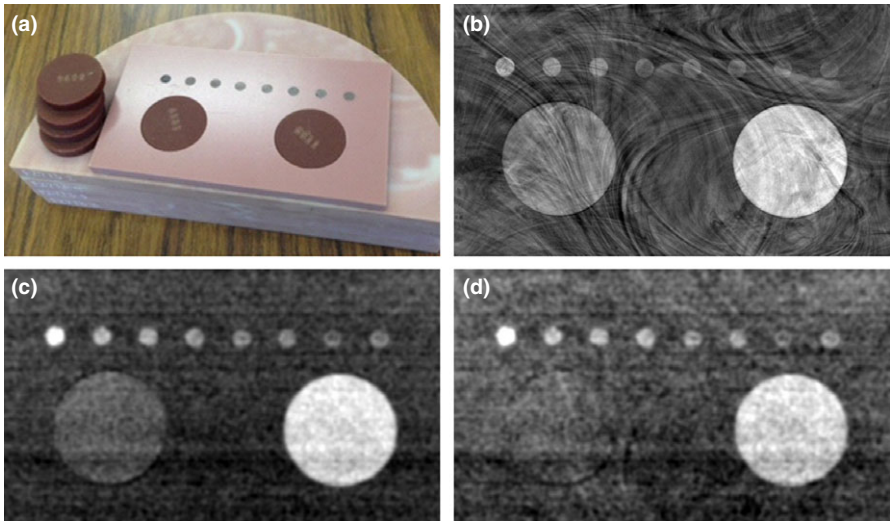


FIG. 6. (a) A photo of the iodine disk phantoms and the BR3D background phantoms; (b) to (d) Log-transferred image of iodine phantoms embedded in BR3D breast phantoms imaged with single-energy (b), dual-energy nonlinear decomposition (c), and dual-energy weighted linear subtraction (d). The large iodine phantoms have mass thickness of 2.5 and 10 mg/cm$^2$. Some small iodine phantoms with a diameter of 5 mm are also shown on the top of the image. Their mass thicknesses vary from 0.4 to 10 mg/cm$^2$. [Color figure can be viewed at wileyonlinelibrary.com]

variation induced by background thickness has been removed. As shown in Table I, the conversion slope depended strongly on the background phantom thickness. For example, when thickness increased from 2 to 5 cm, the slope increased by a factor of approximately 1.5.

The conversion slope, which is used to calculate the final iodine thickness in a lesion, can be affected by the potential uncertainty in background tissue thickness estimation due to iodine uptake. However, the error induced by normal tissue uptake is not a trivial calculation in this method because the total enhancement signal ($S$) in the lesion is also affected by the normal tissue uptake. The result of the sensitivity study is shown in Fig. 10. In general, the error in iodine quantification increases as the background thickness error goes up. However, even with an uncertainty of 40% (16 mm) in background thickness, the iodine quantification error was approximately 0.45 mg/cm$^2$, which corresponds to 9% for the averaged iodine mass thickness used in the study (5 mg/cm$^2$). Another approximate estimation of the potential error can be made using the experimental results from the phantom study. The measurements from 1.25 and 2.5 mg/cm$^2$ iodine phantoms can be used to simulate the background with normal tissue uptake and the lesion in the clinical situation, respectively.[19] Note that the same iodine uptake should be assumed in the normal tissue above and below the lesion. Therefore, the actual mass thickness of iodine in a lesion was approximately 1.25 mg/cm$^2$. The conversion slope can now be calculated using the total thickness measured on top of the 1.25 mg/cm$^2$ iodine phantom, representing the potential normal tissue uptake in the background. The final iodine mass thickness in the lesion phantom derived using the proposed method was determined to be 1.1 mg/cm$^2$, which was in a

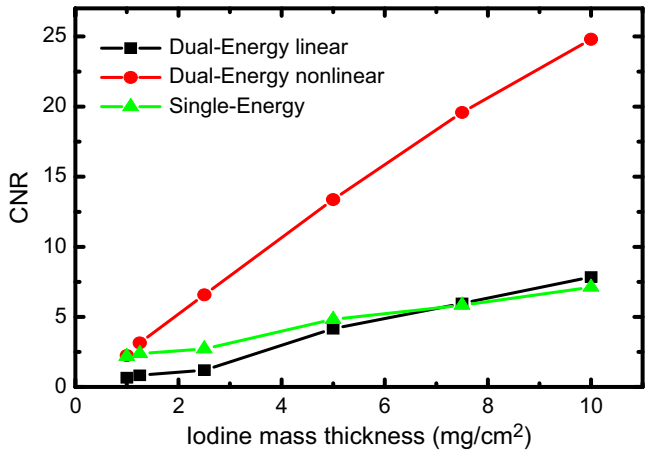


FIG. 7. CNR as a function of iodine mass thickness for single energy and dual energy using both linear log subtraction and the proposed nonlinear decomposition function. [Color figure can be viewed at wileyonlinelibrary.com]

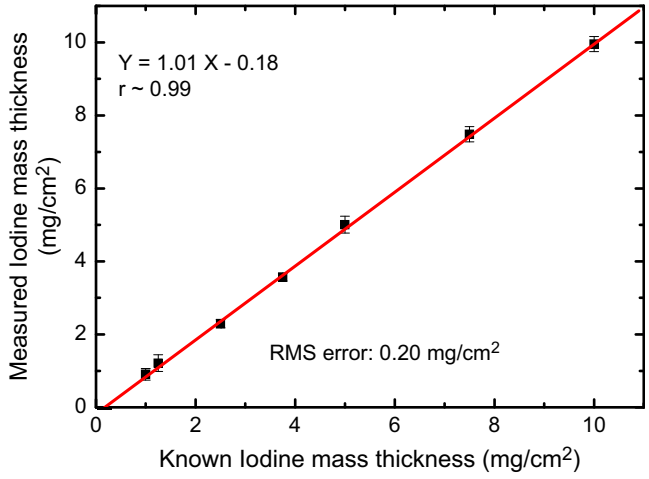


FIG. 8. The measured iodine mass thickness using the proposed quantification method as a function of the known values. [Color figure can be viewed at wileyonlinelibrary.com]

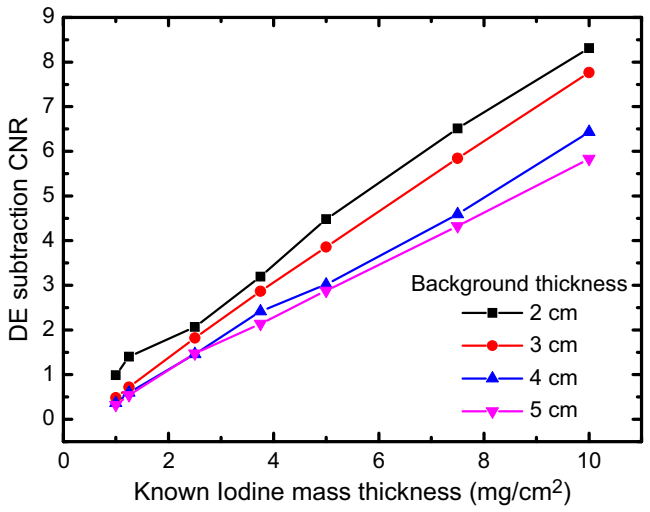


FIG. 9. The measured enhancement signal using dual-energy weighted linear subtraction method as a function of the known values for different breast phantom thicknesses. [Color figure can be viewed at wileyonlinelibrary.com]

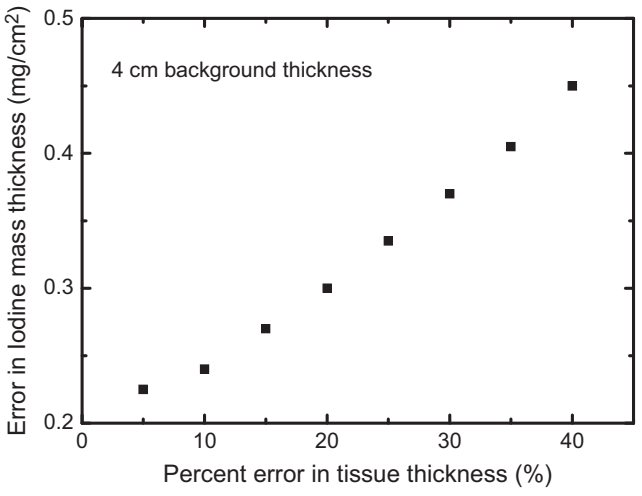


FIG. 10. Iodine quantification error as a function of the percent errors in background thickness estimation for a 4-cm-thick breast phantom.

reasonable agreement with the expected value of 1.25 mg/cm$^2$. Therefore, it can be concluded that the influence of normal tissue uptake can be largely ignored in most cases.

## 4. DISCUSSIONS

In this study, we investigated the feasibility of quantitative characterization of the signal enhancement in contrast-enhanced spectral mammography using a photon-counting spectral mammography system. The selection of the imaging parameters, including tube voltage, splitting energy, and prefiltration, has been optimized in a computer simulation. A phantom study was then conducted using the predicted optimal imaging parameters to validate the proposed quantification method for iodine mass thickness. Current contrast-enhanced spectral mammography technique uses weighted linear log subtraction to minimize the background anatomical noise.[20] However, the linear model is developed based on a monoenergetic input spectrum. The polyenergetic nature of the x-ray spectra used in clinical mammography results in a nonlinear system, where the background noise may not be completely removed using the linear decomposition method.[47] In addition, the conversion method does not calibrate the iodine signal with respect to its true density. As a result, the iodine-induced enhancement signal in the subtracted image depends strongly on the thickness, and the composition of the local breast tissue. As clearly demonstrated in Fig. 7, the same enhancement may correspond to a large range of true iodine mass thicknesses, if breast thickness changes. It is possible to convert this signal into the true iodine density using a lookup table or a system calibration. Puong et al. have proposed a similar method to quantify iodine density using a polynomial fitting function, where the

coefficients are determined through simulations.[48] In the proposed method, all calibrations were done with experimental phantom studies, which accounted for any nonlinear system characteristics that cannot be easily predicted in simulations, such as nonideal detector response and x-ray scatter. The proposed method shares some similarities with the work reported by Puong et al. Both methods used a nonlinear calibration function to convert the dual-energy iodine signal into true iodine density. The surface fitting function used in this study has been reported to have less fitting errors in a previous study on calcification quantification which compares Eq. (7) to polynomial functions.[49] The main innovation of this study lies in the first step of dual-energy decomposition, where the low- and high-energy signals were decomposed into breast thickness and density images, both of which are critical parameters for the accurate quantification of iodine density. All previous methods generally lack a reliable way to measure local breast thickness and density at the site of a lesion. They rely on either compression paddle readings or assumptions about the shape model. Uncertainties in the thickness estimation will result in large errors in iodine density quantification, as we have shown in this study. On the other hand, we have demonstrated in the past that local breast thickness and density can be accurately measured using dual-energy mammography for normal breast tissue without the presence of iodine. This information obtained from normal breast tissue surrounding the iodine-enhanced lesion provides a more reliable estimation of the local breast characteristics. Although current contrast-enhanced spectral mammography techniques may have a reasonable contrast between iodine-enhanced lesion and breast background, it lacks the ability to quantitatively measure iodine density with the desired accuracy and precision. Previous studies have suggested that the contrast-induced enhancement can correlate with certain physiological parameters, such as blood volume and blood vessel density, which are good biomarkers for the differentiation between malignant and benign lesions.[28] Thus, it is necessary to accurately quantify the contrast-induced enhancement, so that this image-based quantitative metric can be used to improve the specificity in breast cancer diagnosis. The proposed quantification method has been tested using breast phantoms with inhomogeneous background patterns. The results suggested that iodine mass thickness can be accurately measured with an estimated error of 0.2 mg/cm$^2$. The accuracy of the measurement does not depend on breast thickness or density. It is thus potentially possible to standardize the contrast enhancement for lesions that appear at different locations in a breast, or those found among different patients. An accurate measurement of the iodine mass thickness, with estimation of the lesion volume from multiple mammography views or reconstructed tomosynthesis slices, can potentially be used to derive blood volume and vessel density inside lesions. Therefore, the neoangiogenically induced vascular changes may be characterized using the proposed quantitative contrast-enhanced spectral mammography. It should also be noted that the application of the proposed method is not limited by the use of the investigated photon-counting spectral mammography system. It can be readily applied to any dual-energy images acquired from conventional mammography systems through a dual-kVp technique.

The goal of our simulation study was to predict the optimal imaging parameters and to understand the loss in FOM due to hardware limitations. To this end, the simulation used most of the hardware settings from a clinical system. In the final result, the optimal tube voltage is slightly less than what has been published for a different mammography system.[20] This is mostly due to the fundamental differences in the detector technology. With the current photon-counting spectral mammography system, the effective attenuation length of the Si-strip detector is approximately 3.6 mm. For high-energy photons, the detection efficiency decreases rapidly as a function of increasing energy. Therefore, the simulated FOM may not benefit much from high beam energies. In the meantime, the employed photon-counting detector separates the low- and high-energy photons in a manner different from the traditional charge-integrating system. With very limited spectra overlap due to the finite-energy resolution of the detector, the FOM will be maximized if the spectrum can be centered around the k-edge of iodine, so that the effective energies in the low- and high-energy spectra are as close to 33.2 keV as possible. This accounts for the fact that when thicker Al filter was introduced, the optimal beam energy was reduced. For an energy-resolved photon-counting mammography system, both low- and high-energy images are acquired within a single exposure. The selected prefiltration material needs to provide a balance between the low- and high-energy photons around the k-edge of iodine. From this point of view, Al is more favorable than other filter materials, such as Mo, Rh, and Cu. The simulation also suggested that the FOM decreased for thicker breasts due to increased dose. One possible solution to improve the FOM is to increase Al filter thickness for thicker breasts, so that a harder beam is used, in this case to mitigate the dose penalty from the low -energy photons.

The FOM simulation suggested an optimal beam energy at 45 kVp. However, the FOM only reduced by 7% when imaging at 40 kVp, which is the current hardware limitation. The 7% reduction in FOM may not be clinically relevant in practice when the absolute value of FOM is considered. As the simulation suggested, there is a broad range of selection for the beam energy around 40 to 45 kVp. By taking advantage of a thick Al filter and the scanning slit geometry, MGD can be reduced to a very low level compared to existing charge-integrating systems. In this case, SNR alone may be more relevant than MGD, as long as MGD follows ALARA. The optimization of SNR is not expected to be very different from that of FOM, as the technique should still be optimized toward a narrow spectrum centered on the k-edge of iodine.

In our iodine quantification technique, the iodine mass is expressed as a function of the measured enhancement signal in the total thickness image, the background breast thickness and density. The breast thickness and density information, however, cannot be directly measured in a lesion due to the presence of iodine in those pixels. Instead, we used

measurements from an adjacent region surrounding the lesion. The assumption is that the total breast thickness and density in the nearby normal tissue are the same as those in the lesion region. This is a reasonable assumption for breast thickness estimations as a large fraction of the compressed breast, which is under the compression paddle, is approximately uniform in thickness. During our calibration, we have found that the conversion slope in Eq. (7) is much more sensitive to breast thickness than density. A 10% error in density and thickness estimation will lead to approximately 0.5% and 46.0% relative errors in iodine quantification, respectively. If the lesion is presented at the breast periphery, the thickness will vary continuously which may affect the accuracy of the iodine quantification. However, the variation in breast thickness can be assumed as smooth and gradual in the periphery. A ring ROI that is carefully delineated around the lesion should still be able to provide a reasonable estimation of the averaged thickness at the lesion site. A more sophisticated approach may also be applied by performing a surface fitting of the thickness signal on the lesion using the measured thickness in the ring ROI as the boundary condition.

In the phantom study, BR3D phantoms with swirl pattern were used to simulate the presence of the anatomical noise in mammography. The introduction of the random background noise with BR3D phantoms is essential to validate our assumptions and to understand the potential error in iodine quantification. However, although the BR3D phantom offers a certain type of noise structure, it is not identical to the anatomical noise in clinical images. Power spectra analysis suggested that the magnitude of the power spectra curves of the BR3D phantom was within the range of clinical images, but the power law exponent ($\beta$) was lower than the average for clinical images.[50] In particular, BR3D phantom has less low-frequency noise as compared to clinical images.[50] Studies based on clinical images for iodine quantification accuracy is currently under investigation in our group. Nevertheless, the proposed quantification method is based on averaged signal over relatively large ROIs. Therefore, the assumptions used in the method should remain approximately true for clinical images.

Finally, although the proposed method was initially developed for contrast-enhanced spectral mammography, its application is not limited to the quantification of iodine signal. In general, the same idea can be applied to quantification of other high contrast signals, such as arterial calcification.[51,52] Studies have suggested that the presence of breast arterial calcifications on mammograms indicates a significantly increased risk of developing coronary heart disease or a stroke.[53] A quantitative measure of breast arterial calcifications through spectral mammography may be viewed as a marker for the development coronary heart disease. For a photon-counting spectral mammography system, this information can be obtained from a standard screening image using this method, without any additional cost or radiation. This method possesses a significant advantage over conventional mammography systems using charge-integrating detectors.

## 5. CONCLUSION

In summary, the optimal imaging parameters for contrast-enhanced spectral mammography were evaluated using computer simulations for a spectral mammography system based on Si-strip photon-counting detectors. Phantom studies were also performed following the simulation guidelines to validate the feasibility of quantifying iodine mass thickness for breasts of various thicknesses and densities. The results show that substantial accuracy and precision can be achieved with the proposed quantification method. Unlike the current implementation of the weighted subtraction method, where the contrast-induced enhancement depends strongly on breast thickness, the proposed method can potentially be used to characterize neoangiogenically induced vascular changes in suspicious lesions. It is thus potentially possible to further improve the specificity in breast cancer diagnosis.

## ACKNOWLEDGMENTS

We would like to thank Daniel Beidokhti and Brian Zhou for their help in data acquisition and analysis. This work was supported in part by NIH/NCI grant R01CA13687.

## CONFLICT OF INTEREST

No conflict of interest or financial disclosures.

[a)]Author to whom correspondence should be addressed. Electronic mail: symolloi@uci.edu; Telephone: (949) 824 5904.

## REFERENCES

1. Nystrom L, Andersson I, Bjurstam N, Frisell J, Nordenskjold B, Rutqvist LE. Long-term effects of mammography screening: updated overview of the Swedish randomised trials. *Lancet*. 2002;359:909–919.
2. Houssami N, Miglioretti DL. Early detection of breast cancer the second time around: mammography in women with a personal history of breast cancer. *Med J Australia*. 2011;194:439–440.
3. Pisano ED, Hendrick RE, Yaffe MJ, et al. Diagnostic accuracy of digital versus film mammography: exploratory analysis of selected population subgroups in DMIST. *Radiology*. 2008;246:376–383.
4. Chiarelli AM, Edwards SA, Prummel MV, et al. Digital compared with screen-film mammography: performance measures in concurrent cohorts within an organized Breast Screening Program. *Radiology*. 2013;268:684–693.
5. Skaane P, Bandos AI, Gullien R, et al. Prospective trial comparing full-field digital mammography (FFDM) versus combined FFDM and tomosynthesis in a population-based screening programme using independent double reading with arbitration. *Eur Radiol*. 2013;23:2061–2071.
6. Mushlin AI, Kouides RM, Shapiro DE. Estimating the accuracy of screening mammography: a meta-analysis. *Am J Prev Med*. 1998;14:143–153.
7. Kopans DB. The positive predictive value of mammography. *Am J Roentgenol*. 1992;158:521–526.
8. Nelson HD, Tyne K, Naik A, Bougatsos C, Chan BK, Humphrey L. Screening for breast cancer: an update for the US Preventive Services Task Force. *Ann Intern Med*. 2009;151:727–737.
9. Kerlikowske K, Zhu W, Hubbard RA, et al. & B. C. S. Consortium. Outcomes of screening mammography by frequency, breast density, and

postmenopausal hormone therapy. *JAMA Intern Med*. 2013;173:807–816.
10. Hubbard RA, Kerlikowske K, Flowers CI, Yankaskas BC, Zhu W, Miglioretti DL. Cumulative probability of false-positive recall or biopsy recommendation after 10 Years of screening mammographyA Cohort Study. *Ann Intern Med*. 2011;155:481–492.
11. Niklason LT, Christian BT, Niklason LE, et al. Digital Tomosynthesis in breast imaging. *Radiology*. 1997;205:399–406.
12. Schmitzberger FF, Fallenberg EM, Lawaczeck R, et al. Development of Low-Dose Photon-counting Contrast-enhanced Tomosynthesis with Spectral Imaging. *Radiology*. 2011;259:558–564.
13. Ning R, Conover DL, Yu Y, Zhang Y, Liu S, Neugebauer J. Koning cone beam breast CT for breast cancer detection, diagnosis and treatment. *Am J Clin Oncol-Cancer Clin Trials*. 2010;33:526–527.
14. Lindfors KK, Boone JM, Nelson TR, Yang K, Kwan ALC, Miller DF. Dedicated breast CT: initial clinical experience. *Radiology*. 2008; 246:725–733.
15. Yang WT, Shaw CC, Chen L, et al. Cone beam breast CT - a feasibility study with surgical mastectomy specimens. *Breast Cancer Res Treat*. 2005;94:S210.
16. Glick SJ. Breast CT. *Annu Rev Biomed Eng*. 2007;9:501–526.
17. Johns PC, Yaffe MJ. X-ray characterization of normal and neoplastic breast tissues. *Phys Med Biol*. 1987;32:675–695.
18. Kuhl CK, Mielcareck P, Klaschik S, et al. Dynamic breast MR imaging: are signal intensity time course data useful for differential diagnosis of enhancing lesions? *Radiology*. 1999;211:101–110.
19. Jong RA, Yaffe MJ, Skarpathiotakis M, et al. Contrast-enhanced digital mammography: initial clinical experience. *Radiology*. 2003;228:842–850.
20. Lewin JM, Isaacs PK, Vance V, Larke FJ. Dual-energy contrast-enhanced digital subtraction mammography: feasibility. *Radiology*. 2003;229:261–268.
21. Cheung YC, Juan YH, Lin YC, et al. Dual-energy contrast-enhanced spectral mammography: enhancement analysis on BI-RADS 4 non-mass microcalcifications in screened women. *PLoS One*. 2016;11.
22. Tagliafico AS, Bignotti B, Rossi F, et al. Diagnostic performance of contrast-enhanced spectral mammography: systematic review and meta-analysis. *Breast*. 2016;28:13–19.
23. Tardivel AM, Balleyguier C, Dunant A, et al. Added value of contrast-enhanced spectral mammography in postscreening assessment. *Breast J*. 2016;22:520–528.
24. Fallenberg EM, Dromain C, Diekmann F, et al. Contrast-enhanced spectral mammography versus MRI: initial results in the detection of breast cancer and assessment of tumour size. *Eur Radiol*. 2014;24:256–264.
25. Dromain C, Thibault F, Muller S, et al. Dual-energy contrast-enhanced digital mammography: initial clinical results. *Eur Radiol*. 2011;21:565–574.
26. Daniaux M, De Zordo T, Santner W, et al. Dual-energy contrast-enhanced spectral mammography (CESM). *Arch Gynecol Obstet*. 2015;292:739–747.
27. Lewin JM, Larke F, Hendrick RE. Dual-energy contrast-enhanced digital subtraction mammography: development and clinical results of a new technique for breast cancer detection. *Radiology*. 2001;221:339.
28. Luczynska E, Niemiec J, Ambicka A, et al. Correlation between blood and lymphatic vessel density and results of contrast-enhanced spectral mammography. *Pol J Pathol*. 2015;66:310–322.
29. Dromain C, Balleyguier C, Adler G, Garbay JR, Delaloge S. Contrast-enhanced digital mammography. *Eur J Radiol*. 2009;69:34–42.
30. Lundqvist M, Danielsson M, Cederstroem B, Chmill V, Chuntonov A, Aslund M. Measurements on a full-field digital mammography system with a photon counting crystalline silicon detector. *Proc SPIE Int Soc Opt Eng*. 2003;5030:547–552.
31. Aslund M, Cederstrom B, Lundqvist M, Danielsson M. Scatter rejection in multislit digital mammography. *Med Phys*. 2006;33:933–940.
32. Aslund M, Cederstrom B, Lundqvist M, Danielsson M. Physical characterization of a scanning photon counting digital mammography system based on Si-strip detectors. *Med Phys*. 2007;34:1918–1925.
33. Aslund M, Fredenberg E, Telman M, Danielsson M. Detectors for the future of X-ray imaging. *Radiat Prot Dosim*. 2010;139:327–333.
34. Bornefalk H, Danielsson M. Photon-counting spectral computed tomography using silicon strip detectors: a feasibility study. *Phys Med Biol*. 2010;55:1999–2022.
35. Fredenberg E, Hemmendorff M, Cederstrom B, Aslund M, Danielsson M. Contrast-enhanced spectral mammography with a photon-counting detector. *Med Phys*. 2010;37:2017–2029.
36. Ding HJ, Molloi S. Quantification of breast density with spectral mammography based on a scanned multi-slit photon-counting detector: a feasibility study. *Phys Med Biol*. 2012;57:4719–4738.
37. Boone JM, Seibert JA. An accurate method for computer-generating tungsten anode X-ray spectra from 30 to 140 kV. *Med Phys*. 1997;24:1661–1670.
38. Nelsona TR, Cervino LI, Boone JM, Lindfors KK. Classification of breast computed tomography data. *Med Phys*. 2008;35:1078–1086.
39. Ducote JL, Alivov Y, Molloi S. Imaging of nanoparticles with dual-energy computed tomography. *Phys Med Biol*. 2011;56:2031–2044.
40. Ding H, Ducote JL, Molloi S. Breast composition measurement with a cadmium-zinc-telluride based spectral computed tomography system. *Med Phys*. 2012;39:1289–1297.
41. Boone JM. Glandular breast dose for monoenergetic and high-energy X-ray beams: Monte Carlo assessment. *Radiology*. 1999;213:23–37.
42. Boone JM. Normalized glandular dose (DgN) coefficients for arbitrary x-ray spectra in mammography: computer-fit values of Monte Carlo derived data. *Med Phys*. 2002;29:869–875.
43. Fredenberg E, Lundqvist M, Cederström B, Åslund M, Danielsson M. Energy resolution of a photon-counting silicon strip detector. *Nucl Instrum Methods Phys Res A*. 2010;613:156–162.
44. Ducote JL, Molloi S. Quantification of breast density with dual energy mammography: an experimental feasibility study. *Med Phys*. 2010;37:793–801.
45. Molloi S, Ducote JL, Ding H, Feig SA. Postmortem validation of breast density using dual-energy mammography. *Med Phys*. 2014;41:081917.
46. Levenberg K. A method for the solution of certain non-linear problems in least squares. *Q Appl Math*. 1944;2:164–168.
47. Contillo A, Di Domenico G, Cardarelli P, Gambaccini M, Taibi A. A novel approach to background subtraction in contrast-enhanced dual-energy digital mammography with commercially available mammography devices: noise minimization. *Med Phys*. 2016;43:3080.
48. Puong S, Bouchevreau X, Patoureaux F, Iordache R, Muller S. Dual-energy contrast enhanced digital mammography using a new approach for breast tissue canceling. *P Soc Photo-Opt Ins*. 2007;6510:U1199–U1210.
49. Kappadath SC, Shaw CC. Dual-energy digital mammography: calibration and inverse-mapping techniques to estimate calcification thickness and glandular-tissue ratio. *Med Phys*. 2003;30:1110–1117.
50. Cockmartin L, Bosmans H, Marshall NW. Comparative power law analysis of structured breast phantom and patient images in digital mammography and breast tomosynthesis. *Med Phys*. 2013;40.
51. Molloi S, Mehraien T, Iribarren C, Smith C, Ducote JL, Feig SA. Reproducibility of breast arterial calcium mass quantification using digital mammography. *Acad Radiol*. 2009;16:275–282.
52. Molloi S, Xu T, Ducote J, Iribarren C. Quantification of breast arterial calcification using full field digital mammography. *Med Phys*. 2008;35:1428–1439.
53. Schnatz PF, Marakovits KA, O'Sullivan DM. The association of breast arterial calcification and coronary heart disease. *Obstet Gynecol*. 2011;117:233–241.